Gucmann, F., Pomeroy, J. W., & Kuball, M. (2021). Scanning thermal microscopy for accurate nanoscale device thermography. *Nano Today*, *39*, [101206]. https://doi.org/10.1016/j.nantod.2021.101206

Peer reviewed version

License (if available):
CC BY-NC-ND

Link to published version (if available):
10.1016/j.nantod.2021.101206

Link to publication record in Explore Bristol Research
PDF-document

This is the author accepted manuscript (AAM). The final published version (version of record) is available online via Elsevier at https://www.sciencedirect.com/science/article/pii/S1748013221001316 . Please refer to any applicable terms of use of the publisher.

University of Bristol - Explore Bristol Research

General rights

This document is made available in accordance with publisher policies. Please cite only the published version using the reference above. Full terms of use are available: http://www.bristol.ac.uk/red/research-policy/pure/user-guides/ebr-terms/

Scanning thermal microscopy for accurate nanoscale device thermography

Filip Gucmann[1], James W. Pomeroy, and Martin Kuball**

Center for Device Thermography and Reliability, HH Wills Physics Laboratory, University of Bristol, Tyndall Avenue, Bristol, BS8 1TL, United Kingdom

Quantitative device thermography, Scanning thermal microscopy, PeakForce tapping mode, Raman thermography, Thermocouple probe, transient heat transport.

*Corresponding Authors

E-mail addresses: filip.gucmann@bristol.ac.uk, filip.gucmann@savba.sk (F. Gucmann), martin.kuball@bristol.ac.uk (M. Kuball)

[1]Present address: Institute of Electrical Engineering, Slovak Academy of Sciences, Dúbravská cesta 9, Bratislava, 841 04, Slovakia

Abstract

We investigate the accuracy and reliability of temperature mapping using scanning thermal microscopy (SThM) in contact and PeakForce tapping mode on the example of a GaN-on-SiC high electron mobility transistor (HEMT). HEMT steady-state and transient surface temperatures are extracted from SThM measurements to study the method's accuracy and transient thermal

response of the SThM probe; the results are verified by 3D finite element thermal simulation calibrated by Raman thermography. A reliable pixel-by-pixel calibration method to convert the measured electromotive force into surface temperature was developed. Discrete point measurements show good agreement (±3°C) with the simulation in both contact and PeakForce tapping modes proving the feasibility of the SThM for accurate device thermography at the nanoscale. However, the measured temperature in calibrated 2D temperature maps deviates by as much as ~15–44% from the simulation, suggesting the SThM probe did not reach the temperature steady state due to limitations in pixel dwell time during the recording of the 2D map.

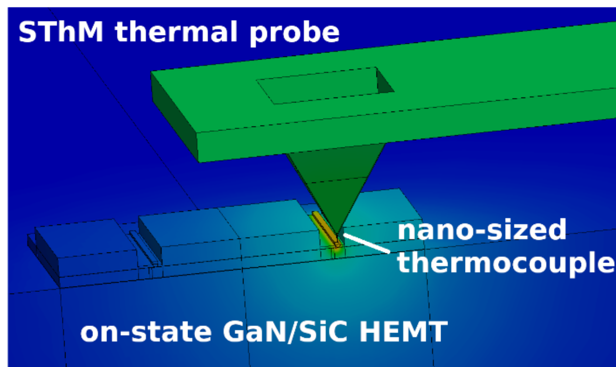

Abbreviations

AFM, atomic force microscopy; SThM, scanning thermal microscopy; FE, finite elements; HEMT, high electron mobility transistor; IR, infrared; PF, PeakForce; TC, thermocouple; FIB, focused-ion beam; EMF, electromotive force; N.A., numerical aperture; W_G, gate width; L_G, gate length; V_{DS}, drain-source voltage; V_{GS}, gate-source voltage; E_a, activation energy; A_c, tip-to-sample contact area; F_c, tip-to-sample contact force; R_{th}, thermal resistance; R_{ts}, tip-to-sample thermal resistance; T_{ch}, maximum channel temperature; ΔT_{ch}, maximum channel temperature rise; T_{Raman}, Raman temperature; T_a, ambient temperature; τ, time constant; R^2, goodness-of-fit.

Introduction

Self-heating of electronic devices is one of the major culprits leading to reduced device performance and potentially severe material degradation, accelerated by high operating temperature, preceding their failure. Comprehensive reliability testing[1–3] is always carried out prior to commercial release of a particular technology to identify weak spots and optimal device operating conditions. For accurate extraction of activation energy (E_a) of a degradation mechanism observed in reliability testing and subsequent device lifetime projections, it is critical to know the true maximum operating channel temperature (T_{ch}) of these devices. In recent years, extensive reliability studies have been carried out on wide band gap semiconductor materials devices, which have attracted much attention due to their advantageous material properties, bringing benefits beyond established material systems, e.g. silicon and GaAs. III-N based electronics is now a mature technology for high power, high frequency, and environmentally challenging applications such as power conversion, transportation, military, aviation, and space. GaN-based III-N high electron mobility transistors (HEMTs) grown on SiC substrates benefit from a reasonable thermal conductivity (160 W/mK for GaN, 450 W/mK for SiC at 300K)[4,5]. Despite this, at high dissipated power densities (typ. ~4W/mm) Joule heating localized at the peak electric field location causes a hot-spot to form, typically at the drain side of the gate contact[6,7]. The size of the hot-spot and related temperature gradients in the surrounding material depend strongly on the used semiconductor materials, device design, and on-state operating conditions. Commonly, GaN HEMT device designs utilize field plates to extend the electric field away from the gate, decreasing the peak electric field, which also helps to partially

mitigate excessive channel temperatures. Typically, most of the Joule heating produced in GaN HEMTs is confined in a layer several tens of nm thick and up to several hundreds of nm long[6].

Existing thermography techniques can severely underestimate the channel temperature, T_{ch}, in GaN HEMTs and similar devices because of their limited spatial resolution. For example, infrared (IR) thermographic imaging is commonly used but the spatial resolution is fundamentally limited by the wavelength of the detected IR emission (several μm), and the IR transparency of many semiconductor materials, which can lead up to 2× underestimation of the ΔT_{ch} in GaN HEMTs.[8] Other frequently used techniques are: Gate resistance thermometry[9–11], making use of the temperature dependence of the gate metal probing the average temperature across the whole gate finger; thermoreflectance imaging[12,13] requiring a complex calibration of the thermoreflectance coefficient for each measured location which can result in accuracies, especially when small features such as gate contacts are probed; Raman thermography[14–16] infers measured temperature from the calibrated temperature-dependent phonon mode shift. This latter method is especially suitable for probing temperature in GaN HEMTs and is considered almost an industrial standard among thermography techniques owing to sub-μm, resolution and ability to probe device temperature close to the peak temperature location. However, even Raman thermography relies on thermal simulation to extrapolate from the measured to the peak channel temperature, typically the difference being 15-40%[8,17–19]. Experimentally calibrated physics-based finite elements (FE) computer simulations are used for this purpose[14,20]. Such calibrated thermal simulation then allows to reliably predict temperature in other parts of the HEMT, e.g. on top of the gate contact[21].

Unfortunately, probing the peak channel temperature directly is experimentally challenging, requiring a higher spatial resolution than the methods mentioned before. Scanning thermal microscopy (SThM), an atomic force microscopy (AFM)-derived thermography technique, has gained significant attention. High spatial resolution (~10-50 nm) temperature maps of various structures were demonstrated[22–31], which is promising for device thermography. SThM relies on surface temperature probing via local nano-scale heat transport between the sample and the sensing element which can typically be a resistor (either actively heated, or in passive mode)[24,27–30,32] or passive nanosized thin film thermocouple[22,23,25,31] as we used in this study, manufactured typically on the apex of the AFM tip. Such probe is held in mechanical contact with the sample, scanned across its surface; both topography and thermal signal, i.e. variations in heating current in case of an active probe or thermal voltage (referred to as electromotive force, EMF) in case of a passive probe is recorded and visualized. SThM measurement was previously demonstrated in contact[25,27,29,31] and tapping mode[26,33], however, PeakForce (PF) tapping is now standard for many other scanning probe microscopy modes. PeakForce tapping combines benefits of contact and tapping mode AFM by allowing for direct force control while avoiding the effect of lateral forces. Unlike tapping mode AFM, PF tapping cantilever oscillations are carried out well below (typically 1-10kHz) cantilever resonance frequency removing constraints of mechanically resonating system. This way, the AFM imaging is insensitive to the Q-factor of the cantilever and cantilever tuning/re-tuning due to the temperature or environmental changes is no longer necessary. Further, unlike in force volume technique, z-position is modulated by sinusoidal signal instead of triangular and thus eliminating resonances at turnaround points[34,35].

In this study, we developed a universal SThM calibration routine for reliable device temperature measurements, which aims to mitigate some of the typical uncertainty sources, and cross-validated it by Raman thermography as industrially established device thermography technique. We tested the pixel-by-pixel temperature calibration of SThM in contact mode and extended it to PF tapping mode. This allowed us to acquire quantitative surface temperature measurements of the on-state GaN HEMT in both SThM modes in the form of either 2D temperature maps or discrete points.

To explain observed 15-44% temperature discrepancies found for calibrated 2D temperature maps, we study the thermal dynamics of the SThM probe and assess its practical implications for temperature measurements by means of transient SThM and transient thermal simulation.

Measurement uncertainty in scanning thermal microscopy

The SThM concept although very elegant in design, may suffer from measurement uncertainties. Typical sources of SThM measurement uncertainty are: ***1) Tip-to-sample contact area (A_c) variation*** that results from roughness of the sample surface (larger A_c in pits, smaller on top of hills) and corners of device features manifesting as artefacts showing higher/lower temperature deviating from reality. ***2) Tip-to-sample contact force (F_c) variations*** represented by the chosen setpoint of the SThM measurement, related to the magnitude of force exerted by the tip on the sample surface and maintained by the tip height controlling feedback. As opposed to tapping and PeakForce tapping mode, contact mode SThM benefits from higher F_c and thus improved heat transport. However, the higher the F_c, the faster the SThM tip deformation and wear is, consequently increasing A_c during the measurement. From this point of view, PeakForce tapping mode allowing for F_c as low as few pN[34,35], as compared to tapping mode (~1 nN[35]) and

contact mode (10s-100s nN[36]), offers the best performance, also documented by enhanced tip control enabling atomic resolution in AFM scanning[34]. ***3) Parasitic heat transport mechanisms.*** Heat conduction via the point of contact between the probe and the sample is expected to be the dominant heat transport mechanism in SThM. However, when scanning in ambient air and pressure, presence of water meniscus surrounding the tip at the point of contact not only hinders the lateral resolution, but also enables additional heat convection to the tip[37,38]. This effect is temperature dependent; it is reduced at temperatures close to water boiling temperature, and can be further reduced or completely mitigated by introducing of dry inert atmosphere (N, Ar) or vacuum, respectively. In some cases, heat conduction through the surrounding air can affect the temperature readings: Heat conduction through the air volume surrounding the probe vs through the nanoscale thermal contact may cause a parasitic heat transport. Suitable probe designs and measurement at moderate temperatures help mitigate this issue, while measurement in vacuum removes this problem completely [38]. Radiative heat transport is usually of little concern when moderate temperature (<200 °C) samples are probed [38], however can severely degrade the lateral resolution at higher temperatures when other parts of the probe and cantilever can absorb significant amount of heat. ***4) Material-related phonon mismatch variations***[39–41] at the point of tip-to-sample contact affecting the heat conduction. All these constitute a varying, measurement-location-specific, tip-to-sample thermal resistance (R_{ts}), impacting the ability to accurately measure temperature using SThM. Any reliable SThM temperature calibration methodology must be able to account for varying R_{ts} to prevent erroneous readings and widely observed temperature artefacts. A very important, yet typically less discussed factor influencing SThM measurements is ***5) transient heat flow between sample and the tip***, since reliable temperature readings require the sensing element, in our case a

nanoscale thermocouple (TC), to reach the steady state before the temperature is recorded. The time scale for the TC junction to reach the temperature steady state is significantly affected by R_{ts} and other thermal resistance (R_{th}) contributions presented by the rest of the SThM probe and cantilever. Understanding of transient thermal behavior of the SThM probe (TC junction) is essential for reliable acquisition of high-resolution 2D temperature maps since the TC junction is required to reach the steady state at every measurement location/pixel, otherwise measured temperature will be under/overestimated depending on positive/negative temperature difference between consecutively measured pixels.

Experimental and simulation details

A Bruker Dimension Edge atomic force microscope (AFM) platform and scanning thermal microscope setup manufactured by AppNano equipped were used, consisting of VertiSense control and signal processing add-ons, and customized VTP-200 thermal probes. All measurements were carried out in ambient atmosphere; a protective enclosure was used for noise isolation and to avoid environmental temperature perturbations. VTP-200 is a passive SThM probe, which has a nano-sized, thin metal film thermocouple manufactured on the top of a hollow SiO_2 pyramid, located at the end of 200μm long and 50μm wide Si cantilever. Typical spatial and temperature resolution is ~50nm and ~0.04°C, respectively, with operating temperatures as high as ~700°C [23,42]. Details of the probe manufacturing process and probe capabilities can be found elsewhere[23,43]. Typically, the scanning metallic nanowire tip of the SThM probe connected to nano-sized TC junction protrudes up to several hundreds of nanometers above the SiO_2 pyramid apex. Here we used customized probes where the length of

scanning metallic nanowire protrusion was in range of few micrometers. This was achieved by precise focused ion beam (FIB) milling of the probe tip enabling to study high aspect ratio surface features of GaN HEMT without compromising the spatial resolution in trenches. Due to the prolonged scanning needed to acquire 2D temperature maps with corresponding calibration data, some degree of tip wear cannot be ruled out and we estimate the tip radius/tip contact area was ~50-100nm. Schematic cross-section of the used probe is shown in Fig. 1. The devices studied were passivated two finger unpackaged (on wafer) GaN/SiC HEMTs (W_G = 50μm, L_G=0.25μm), which were operated at dissipated power densities in the range of 2 – 12W/mm. Only one half of the device, i.e. one gate finger was operated. We note dissipated power density in W/mm is used, which corresponds to the power in W divided by the total HEMT periphery (number of gate fingers times gate width W_G) in mm. Measured temperature-dependent electromotive force (thermal voltage) was amplified and fed to the input port of I/O bus of the AFM. NanoDrive software was used to route the EMF signals within the instrument and enabled data acquisition and visualization.

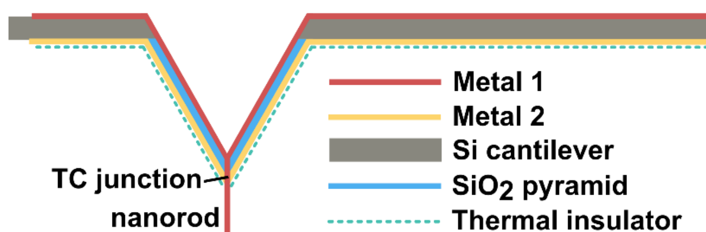

Figure 1. Schematic cross-section of the customized VTP-200 passive SThM probe (not to scale). Protrusion of the scanning nanorod was on order of a few μm to achieve sufficient spatial resolution in trenches of HEMT access regions. The thermocouple, TC, junction is formed at the point of contact between two different metal layers.

SThM measurements were performed in contact and PeakForce tapping modes. The main difference between the two modes is that when scanning in contact mode, the probe is in continuous contact with the sample surface, i.e. tip-to-sample distance is set exclusively in the range of short-range repulsive inter-atomic forces (see Fig. S1). In contrast, in PeakForce tapping mode, the tip-to-sample force working window spreads out towards the range of attractive inter-atomic forces, while aiming to maintain a slightly repulsive force mode at the point of contact with the sample (see Fig. S1). Here, the probe is in an intermittent contact with the sample during scanning, alleviating tip wear and eliminating lateral tip forces. The most important difference between the traditional tapping and PeakForce taping mode is that while the former requires the cantilever to operate at its mechanical resonance (typ. 10s – 100s kHz) and does not allow for direct tip-to-sample force control, the latter operates at tapping frequencies well below cantilever resonance and allows for force to be controlled via peak force settings, allowing to reach pN scale.

Fig. 2 shows the measured transient cantilever deflection corresponding to the transient force signals for various setpoint values (0.5 – 3V) in PeakForce tapping mode at 2kHz piezo oscillation frequency; the inset shows approximate contact times as a function of PF amplitude (probe travel distance during each tapping cycle) derived from transient PF signals. Tip-to-sample approach and withdraw is carried out at every pixel measured and probe vertical movement is described by the sine function reaching minimum for corresponding peak contact force. Typically, PeakForce tapping uses ScanAsyst[34] – an automated feedback PID gains and PF setpoint adjustment. While this can greatly improve topography scans, the setpoint is directly related to the maximum force exerted on the sample surface by the probe and thus the mechanical contact. If this varies, R_{ts} varies too, affecting the time required for SThM probe to

reach the steady state which can in turn significantly affect the measured EMF. While the setpoint-induced EMF variation in contact mode SThM can be negligibly small (~2% in setpoint range 0 – 3V), errors as high as ~25% of measured EMF may be introduced in PeakForce tapping mode if not carefully chosen (See Fig. S2). Therefore, automatic setpoint adjustment was switched off in all our PeakForce tapping SThM measurements and a constant value 3V was chosen as an optimal trade-off between good mechanical contact and SThM tip wear. Tip-to-sample contact time in range of ~170 – 310μs per one approach/withdraw cycle were chosen. We note, the contact force varies by design during PF approach/withdraw cycle and is not represented by the single peak contact force value.

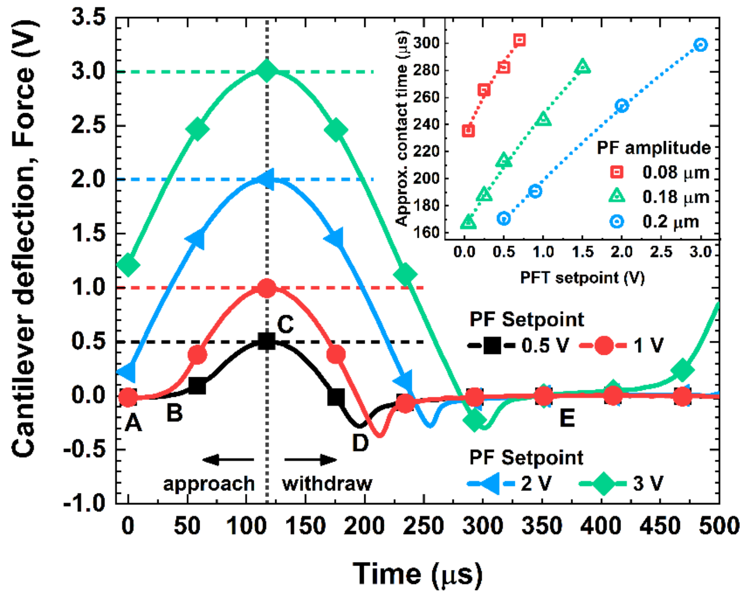

Figure 2. Experimental transient cantilever deflection/force signals as a function of PF setpoint. A, B, C, D, and E, respectively, designate start of the approach, jump into contact, peak contact force, contact adhesion at the start of withdraw, and complete probe withdraw. Tip is considered to be in contact with the sample between points B and D. Inset shows approximate times probe is

in contact with the sample surface as a function of PF setpoint and PF amplitude. Trend lines serve as a guide to the eye.

To quantify the accuracy and limitations of SThM, first, a steady-state 3D thermal FE computer model representing the GaN/SiC HEMT was created according to its physical dimensions and used materials and experimentally verified using Raman thermography. After this, a SThM measurement was used to acquire device on-state 2D EMF maps and EMF signals for several discrete points along the passivated gate contact, and corresponding temperatures and temperature maps were calculated using pixel-by-pixel calibration method and cross-compared with the thermal model of the GaN/SiC HEMT from the previous step. Subsequently, the thermal time constant of the SThM probe used was experimentally determined by transient SThM measurements while the device was operated in pulsed mode; this was used to validate the transient thermal simulation of the SThM probe. Next, another transient thermal simulation was performed, combining the verified steady-state thermal model of the GaN/SiC HEMT and the verified transient thermal simulation of the SThM probe. Transient heating of the probe was simulated for several consecutive probe displacements, i.e. pixels, along the HEMT gate contact for various pixel times. This is illustrated in the chart S1 in supplementary material.

Results

1. GaN/SiC HEMT steady-state thermal model verification

For the steady-state 3D thermal FE model representing the GaN/SiC HEMT, half of the device was simulated owing to its symmetry; temperature-dependent thermal conductivities (κ) of each material used in the simulation are given in Table S1 in the supplementary material. We note, where appropriate, used reported values of temperature-dependent thermal conductivities of thin layers are much lower than for bulk materials accounting for the size effects. The finite size of the heat source in the GaN layer (0.5µm) and the thickness of the GaN layer (2µm) is much larger than the phonon mean free path (MFP) in GaN (~100nm)[44]. Therefore, in this case reduction of the effective local thermal conductivity of GaN is not expected. However, this effect should be considered in the nanoscale device modelling, where hot spot is smaller than phonon MFP.

This model was validated using Raman thermography measuring a device in the on-state, using a Renishaw InVia confocal Raman spectrometer with 532nm laser excitation source, 50× 0.5 N.A. objective lens (laser spot size ≈0.5µm), and thermoelectric microscope chuck for maintaining a constant ambient temperature (T_a=25°C), using the A_1(LO) GaN phonon mode for temperature measurements. During the temperature measurement, the transistor was operated at dissipated power density (P_{diss}) of 2–12W/mm with applied constant source drain voltage of V_{DS}=10V. Raman temperatures (T_{Raman}) were recorded 0.5µm away from the drain edge of the T-shape gate contact in the center of the device, where the temperature is the highest, as well as 300µm away from this location. The latter was found equal to the set thermal chuck temperature confirming

good thermal contact and no temperature difference between the chip and chuck. Further information on this technique can be found elsewhere[14–16].

Fig. 3 shows experimental and simulated T_{Raman} vs dissipated power density, and maximum channel temperature which was extrapolated from measurement using the simulation. Schematics of device cross-section demonstrating Raman probed volume is shown in Fig. S3 in the supplementary material. The simulated T_{Raman} was in a good agreement with the experimental values, well within the instrumental uncertainty (±5°C). This verified FE model was later used to extract device surface temperatures at locations probed by SThM used for thermal calibration of the SThM probe.

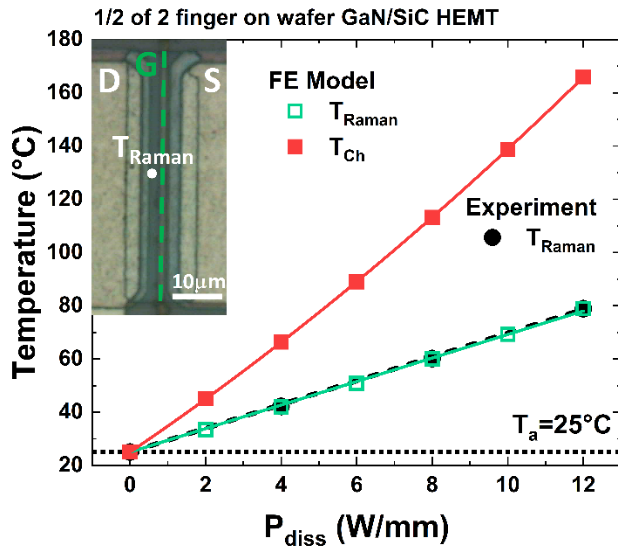

Figure 3. Experimental and simulated Raman temperature, T_{Raman} vs dissipated power density, and maximum channel temperature, T_{ch}, extrapolated from verified FE model of ½ of two finger GaN/SiC HEMT operated at ambient temperature of 25°C. Inset shows T_{Raman} measuring location – drain side of the center of gate contact.

2. Pixel-by-pixel calibration methodology

To improve the accuracy and mitigate some of the SThM temperature measurement uncertainties, we developed a pixel-by-pixel calibration methodology, which can be universally applied in the 2D temperature mapping, 1D line temperature profiling, and in discrete point temperature measurements.

We illustrate this method on an example of 2D temperature mapping of GaN/SiC HEMT, results of which are presented it the next section. In that case, the calibration routine consisted of recording of consecutive off-state (no dissipated power density in the device channel) 2D EMF maps of the same device area at various ambient (backplate) temperatures (25-60°C). A vector holding these measured EMF values was created for each measured pixel of the acquired 2D map. EMF as a function of set ambient temperature was approximated by linear regression for each pixel and corresponding fitting parameters, i.e. intercept, slope, standard error of the estimate, and R^2 value (goodness-of-fit) were extracted. In the next step, the on-state temperature map of the device was determined using corresponding on-state EMF map of the same device area by pixel-by-pixel calculation assuming $T(V) = a \times EMF + b$, where a and b are respective values of slope and intercept at each pixel determined from previously described linear regression of the calibration data.

This calibration is location-specific, i.e. needs to be carried out over the area where the surface temperature is investigated. This results in its sensitivity to the sample drift. Therefore, compensation for the influence of the thermal expansion is important and closed-loop scanning is preferred. More information on this technique is available in the supplementary material.

3. 2D temperature mapping using SThM

The topography and corresponding temperature map of the GaN/SiC HEMT are shown in Fig 4 a) – d). As the scans were recorded in the center of the device, temperature gradients along the gate width direction were negligible. To improve the accuracy of 2D temperature mapping in contact mode, we applied the pixel-by-pixel calibration methodology described in the previous section to the measured 2D EMF maps of the center (11×11μm) of passivated GaN/SiC HEMT in the on-state, operated at P_{diss}=8W/mm. Calculated standard error within 1°C and R^2 values >0.996 for each pixel support suitability of this approach. 2D maps of these quantities are available in the supplementary material (Fig. S4).

The granular texture of the source and drain metal plating (~1°C higher temperature between adjacent metal grains) is clearly visible in Fig 4, as is an elliptical feature (~7°C lower temperature) adjacent to the gate contact at the drain side in the top section (Fig. 4 b)). These appear to be contact area variation-related (i.e. topography-related) artefacts. Pixel-by-pixel calibration method should be in theory able to eliminate topography-related artefacts by maintaining constant contact force and area for calibration and temperature measurement. Possible explanation for topography-related artefacts may be minor gradual tip wear affecting the contact area.

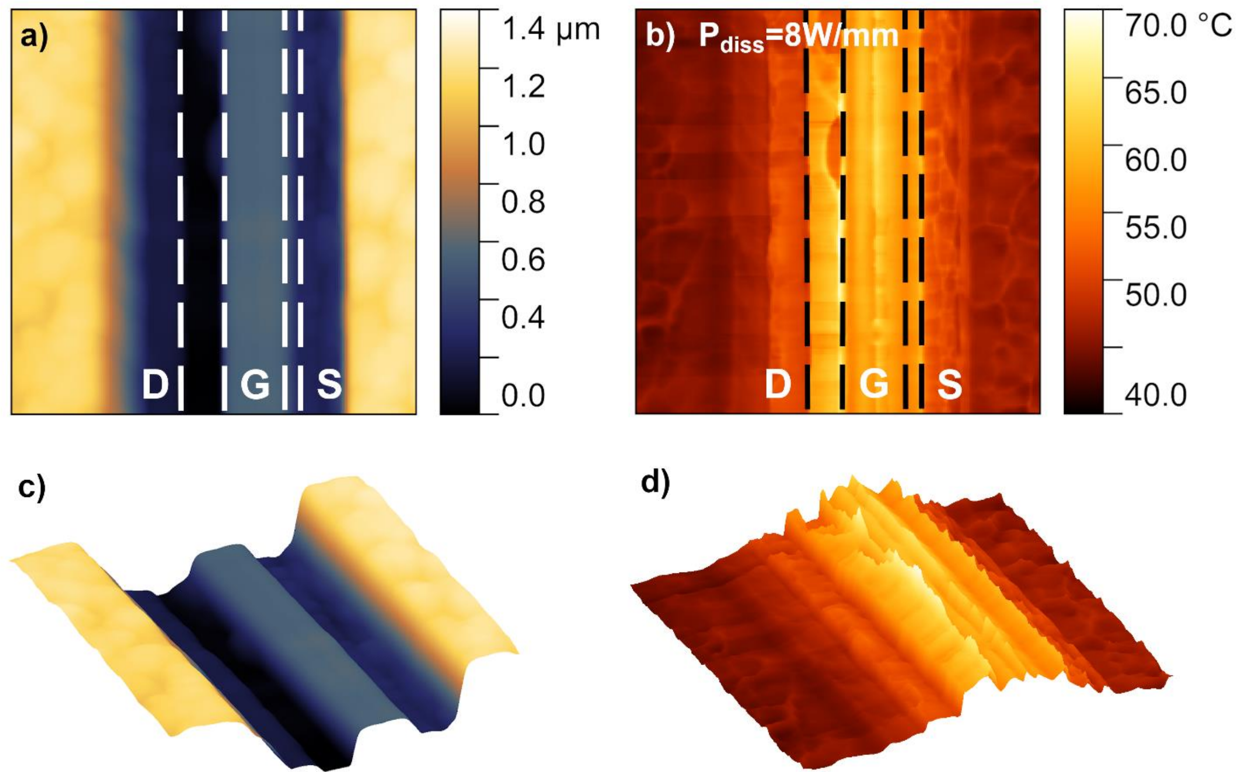

Figure 4. Planar a) – b) and 3D c) – d) representation of topography and corresponding temperature map of GaN/SiC HEMT operated at P_{diss}=8W/mm. Temperature map was determined using pixel-by-pixel calibration of the VTP-200 SThM probe. Scan size is 11×11µm. D, G, and S denote drain, gate, and source contacts, respectively.

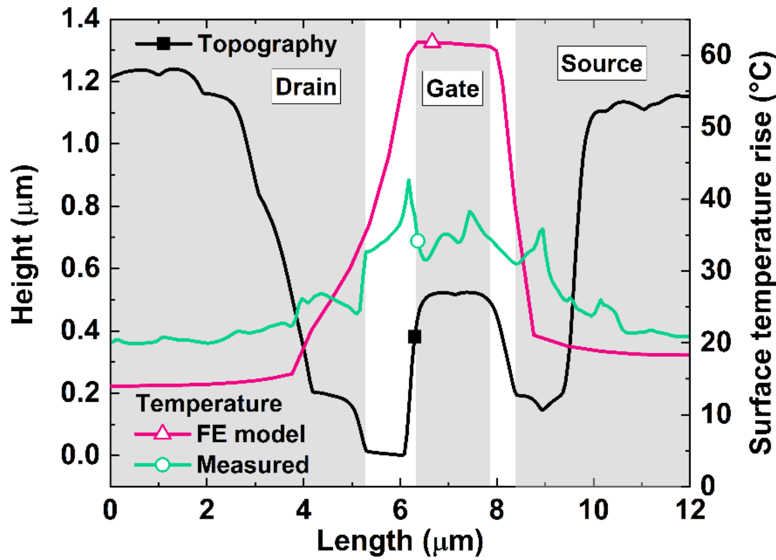

Figure 5. Measured topography and calibrated surface temperature rise profiles at the device center taken from Fig. 4 a) and b). Corresponding simulated surface temperature rise profile is shown for comparison.

Fig. 5 depicts measured line profiles from the center of the studied GaN HEMT – topography and corresponding SThM surface temperature rise with respect to the ambient temperature T_a=25°C, taken from Fig. 4 a) and b), respectively. The simulated surface temperature rise is overlaid for comparison, which was extracted from steady-state thermal simulation at the same location. The measured temperature rise deviates significantly from the simulation on top of the gate contact, i.e. ~44% lower than simulated, whereas the measured temperature rise is ~15–25% higher on the source and drain metal. The observed discrepancy between measured vs simulated temperature rise indicates the SThM probe may not have reached the temperature steady state even for the slowest scanning settings. However, other factors may also contribute to this discrepancy. Since the probe in contact mode AFM is in continual motion (does not dwell at

each pixel) during scanning, the vertical force feedback maintaining the chosen setpoint (i.e. contact force) is constantly actuating inducing changes in mechanical tip-to-sample contact and affecting the heat flow.

4. Discrete point temperature measurement using SThM

To address the observed 2D SThM temperature mapping temperature discrepancy, EMF was measured in contact and PeakForce tapping mode along the width of the top of the passivated gate contact but at 6 discrete locations: 0, 5, 10, 15, 20, and 25μm where 0=the gate edge and 25=gate centre; now keeping the tip stationary during each measurement, averaging the EMF signal for 10s (8000 samples at ~1Sa/1ms). The device was operated in the on-state, at P_{diss}=4, 6, and 8W/mm. Pixel-by-pixel SThM probe calibration as described previously was carried out for each one of these measured locations. The resulting determined surface temperatures are shown with the overlaid simulated steady-state surface temperature profiles in Fig. 6. The FE model, contact and PeakForce tapping mode measurements now agree within ±3°C. Some discrepancies observed close to the edge of the gate contact are likely related to minor thermal drift unaccounted for and slight differences in the geometry of the modelled GaN/SiC HEMT compared to the real case, e.g. influence of the gate pad dimensions affecting the heat spreading outside of the device. Overall, this confirms that during SThM mapping the steady state is not reached but point measurements can achieve accurate temperature measurements.

The good agreement of experimental SThM surface temperatures with the model shows the suitability of this method for (nanoscale) device thermography. Accuracy of Raman thermography-calibrated steady-state FE thermal model achieves typically ±5°C. SThM can complement Raman thermography; the accuracy of thermal models can be improved by SThM

providing additional temperature measurements, or probing temperature in locations or devices otherwise inaccessible by Raman thermography.

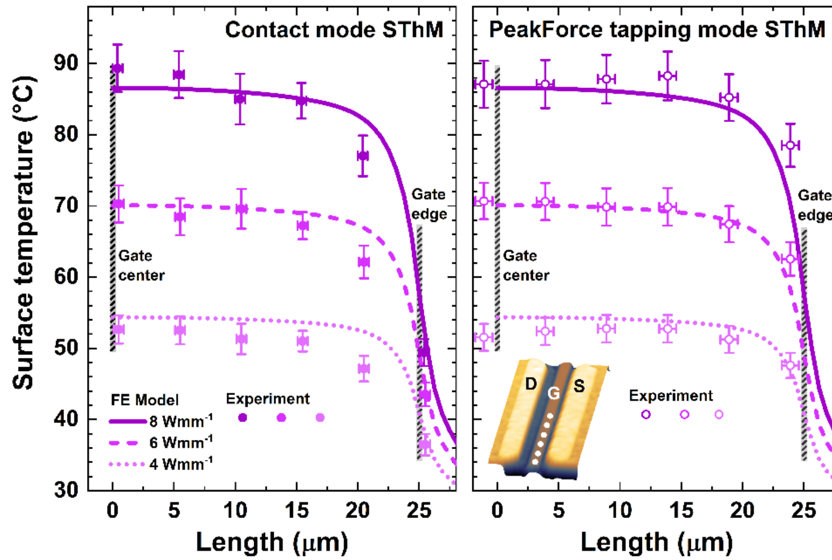

Figure 6. Surface temperature along the passivated gate contact of on-state GaN/SiC HEMT operated at P_{diss}=4, 6, and 8W/mm determined from measured EMF signals in contact and PeakForce tapping mode using pixel-by-pixel calibration overlaid on steady-state FE model data. Inset illustrates measured locations. Temperature error bars were calculated assuming error propagation formulas considering standard error of the measured EMF and errors associated with intercept and slope of the linear regression trend lines used to approximate the calibration data; largest error was about ±3°C. Position (x-axis) error bars are associated with temperature drift of the system and are larger in case of PeakForce tapping SThM as lateral scan linearizing signals were switched off in this case, to gain free data bus channel allowing measured EMF to be recorded.

5. Temperature steady state of a SThM probe

For accurate high-resolution 2D temperature maps, SThM probe is required to reach the temperature steady state at each pixel of the scanned area. In an ideal case of a sufficiently planar surface and small temperature differences between adjacent pixels, tip-to-sample contact time per pixel in contact mode can be estimated as the time needed for the probe to travel between two adjacent pixels. In our case (scan size 256×256px – 512×512px, time per scanned line 2.5 – 5s) this was approximately in range 4.9 – 20ms. For PeakForce tapping, however, this is about one order of magnitude shorter (~170 – 310μs). In order to evaluate the time required for the probe to reach the steady state, a transient FE thermal model of the VTP-200 SThM probe was built; this was verified using a transient temperature measurement carried out on the same GaN/SiC HEMT as used in the Raman thermography measurement. During the measurement, the SThM probe was placed on the top of the passivated gate contact in the center of the device and transient EMF signals in contact mode were recorded. The transistor was operated at P_{diss}=8W/mm with applied constant source drain voltage of V_{DS}=10V, whilst the gate was pulsed from pinch-off to V_{GS}=-1.9V for 240ms with 50% duty cycle allowing the device and SThM tip to reach the steady state at the end of each half period.

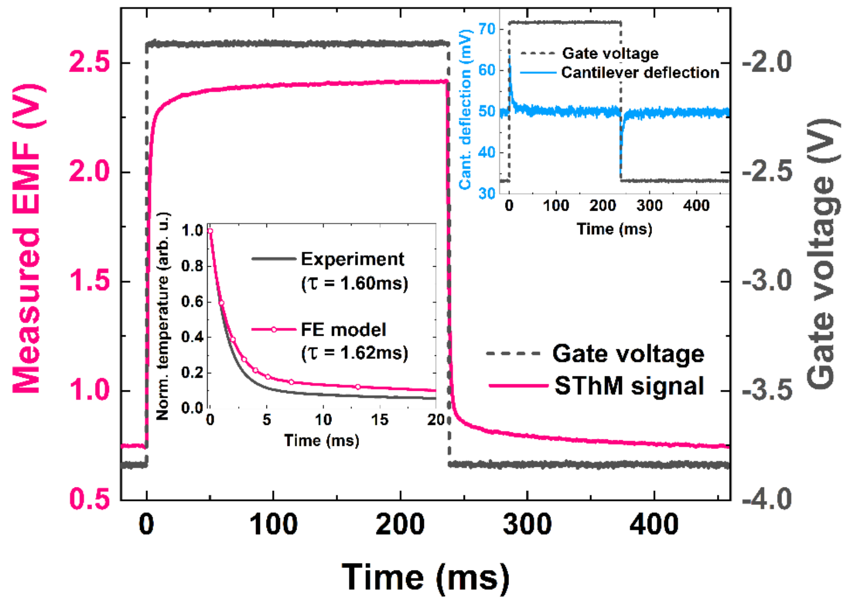

Figure 7. Experimental transient EMF trace of GaN/SiC HEMT measured on top of the passivated gate contact in the center of the device for one pulse period with corresponding gate voltage trace. Shown in inset (left) is detail of normalized transient thermal voltage for first 20ms of the cool-down half period (pinch-off) and the best fit result with the transient FE model. Second inset (top right) shows transient cantilever deflection trace during one pulse period.

Figure 7 shows the measured transient EMF signal and corresponding gate voltage pulse, which is compared to the transient thermal model. This transient 3D FE thermal model comprised of a simplified GaN heater (6.5×1000μm) on SiC substrate (thickness of GaN and SiC were the same as in case of measured GaN-on-SiC HEMT). Electrical power applied to the heater was chosen so its maximum temperature was similar to the temperature of the previous GaN/SiC HEMT steady-state FE model at the corresponding location; the thermal probe FE model used dimensions and materials for VTP-200 supplied by the manufacturer (Si cantilever:

w×h×l=50µm×3.5µm×200µm; square base hollow SiO_2 pyramid)[42] and determined from FIB cross-sectioning. Reported platinum material properties (see Table S1 in supplementary material) were used; a 1.5µm long protruding nanorod with 100×100nm rectangular base served as a scanning element of the probe. Figure 8 shows SThM probe used in transient thermal simulation, detail of the element representing the R_{ts}, and the location of TC junction. Also shown is a schematic of the equivalent thermal circuit of the system. We note this schematic is only illustrative as, for simplicity, single time constant was used to approximate the transient EMF trace and corresponding simulated transient temperature trace. A cube element with the side of 100nm was placed in between the heater surface and the nanorod at its end, representing R_{ts}. Thermal resistance of the cube element and the volume of Pt infill inside the pyramid was varied to approximate the thermal mass of the probe and to match the measured EMF transient as closely as possible. We assumed EMF readings reflect the TC junction (point of contact of two metal films forming the junction) temperature; a rectangular area with side length of 100nm at the top end of the nanorod, where it meets the pyramid was considered TC junction in the model. The average transient temperature over this area was adjusted to meet the experiment. Due to their negligible contribution, radiative and convective heat transport were not assumed in the simulation.

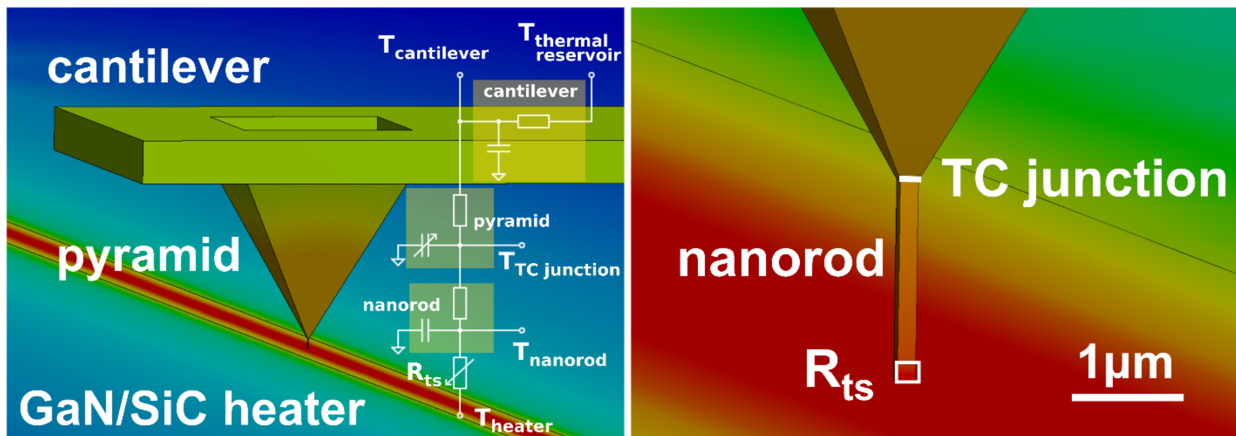

Figure 8. VTP-200 SThM probe used in the transient thermal simulation to match the probe thermal time constant. Locations of tip-to-sample thermal resistance, R_{ts}, and thermocouple, TC, junction, and corresponding illustrative equivalent thermal circuit are also shown.

Best agreement with the experiment was achieved for tip-to-sample thermal resistance $R_{ts} \approx 0.7\times10^{8}$K/W, comparable to results (~1.5-2×10^{8}K/W) previously reported by Kim and Shi[22,45]. The extracted best-fit simulated time constant value τ=1.62ms is in good agreement with the experimental value of 1.60ms. The time constant in the millisecond range is a manifestation of the thermal response of the SThM setup, as the expected thermal time constants for the GaN HEMT itself has been reported to be one order of magnitude faster[46]. We note that in our simulation, the SThM cantilever was assumed thermally floating, whereas in the real case there is always some heat flowing out to the cantilever holder and the AFM chassis, which may result in some overestimation of the time constant in the simulation. The inset of Fig. 7 shows the cantilever deflection spikes around points where temperature changes the most, showing the effect of thermal expansion on the sample and the probe. This suggests the AFM feedback needs to actuate the probe to maintain the chosen setpoint, which may consequently temporarily change the contact force resulting in temporal changes in sample to tip heat flow rate affecting the measured EMF.

For most of practical applications, reaching of a steady-state can be assumed to be reached for times >4×τ (assuming exponential growth/decay) as this corresponds to reaching >98% of the steady-state value. Assuming the experimentally determined SThM probe time constant, 4×τ=6.4ms would be the minimum time required for the probe to spend on each pixel when

recording a 2D EMF map to reach the steady state and accurately record surface temperature. This condition may have been met for contact mode SThM measurement if the probe was not in perpetual motion (estimated time per pixel ~4.9 – 20ms), whereas is was not achieved for the PeakForce tapping mode (~170 – 310μs).

6. Transient thermal response of the SThM probe during scanning

To study the transient behavior of the VTP-200 SThM probe during scanning in the case of investigated HEMT further, the steady-state thermal simulation of the GaN/SiC HEMT was extended with the verified physical model of the probe placed on top of the passivated gate contact (Fig. 9). The simulated HEMT steady-state temperature field corresponded to P_{diss}=8W/mm; the average temperature in the square area representing the TC junction of the probe was determined. Six consecutive displacements of the SThM probe along the half length of the gate contact (i.e. 6 iterations of the model), positioned 0, 5, 10, 15, 20, and 25 μm, i.e. from the gate edge to the gate centre corresponding to the measurement locations shown in Fig. 6., described as "pixels" in the following discussion. The simulated temperature field in the SThM probe at the end of each nth iteration was used as a starting temperature for each $(n+1)^{th}$ iteration. The time the SThM probe spent at each pixel's location was varied to match estimated pixel times of the experimental conditions in contact mode (20, 9.8, and 4.8ms) and best-case scenario for PeakForce tapping mode (0.3ms). The resulting accumulated transient temperature traces for various contact times are presented in Fig. 10; the inset displays the result for 3rd-6th pixels in detail to illustrate deviations from steady-state value at the end of each iteration (displacement). Even for dwell times as short as 4.8ms per pixel, the simulated TC junction temperature eventually reaches the steady-state value (from the 5th pixel onwards). In our

GaN/SiC HEMT experimental scenario, this would happen after several measured pixels so the largest error would occur in the beginning of the scanning and would decrease gradually. However, interpretation of temperature traces in case of mapping of more complex temperature fields, e.g. presence of step temperature changes, becomes challenging. Here we considered the probe starting temperature was 25°C, which may differ from the real experimental case dependent on the position of the probe on the sample relative to the heat source prior to the start of scanning and can typically be higher, i.e. the steady state may be achieved even faster. This transient thermal model result, however, contradicts our experimental observation; 2D temperature mapping consistently measured lower surface temperature than predicted by steady-state FE model for the same range of pixel dwell times considered here. We ascribe this difference mainly to the temperature memory effect SThM probe experiences in case of insufficient pixel dwell time during 2D temperature mapping. AFM feedback may also be contributing factor which limits the reaching of the temperature steady state of the SThM probe within the expected times. Feedback actuates the probe lateral and vertical movement, possibly affecting the tip-to-sample mechanical contact and related heat flow. The simplest solution to overcome this issue in 2D temperature mapping may be to program a probe control routine, forcing a fixed time interval the probe spends per pixel, long enough to reach the steady state before the EMF reading is acquired. An optimal pixel dwell time needs to be found experimentally. Based on our experimental results we estimate dwell times one or two orders of magnitude longer than the most time-efficient case of probe-stepping transient thermal simulation (9.8ms) may be sufficient, i.e. 0.1 – 1s per pixel. A trade-off between scan resolution and length of the 2D map acquisition would be required as e.g. 256×256 scan would take ~2h

and ~20h, while 64×64 scan only ~7min and ~70min for pixel times of 0.1 and 1s, respectively, including the time needed for probe to move between the adjacent pixels.

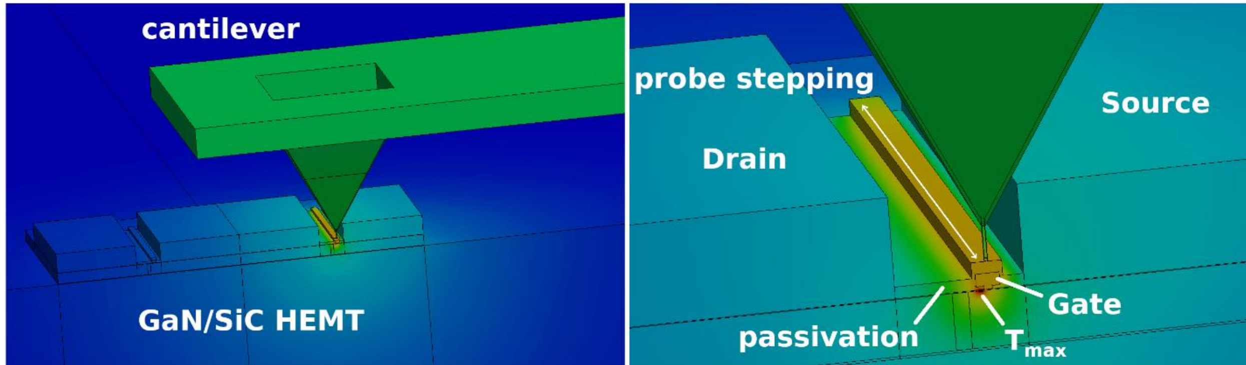

Figure 9. Transient FE model of VTP-200 SThM probe placed on the top of the passivated gate contact of GaN/SiC HEMT. Probe was stepped along the half of the gate length across 6 locations (0, 5, 10, 15, 20 and 25µm) from the gate edge towards gate center.

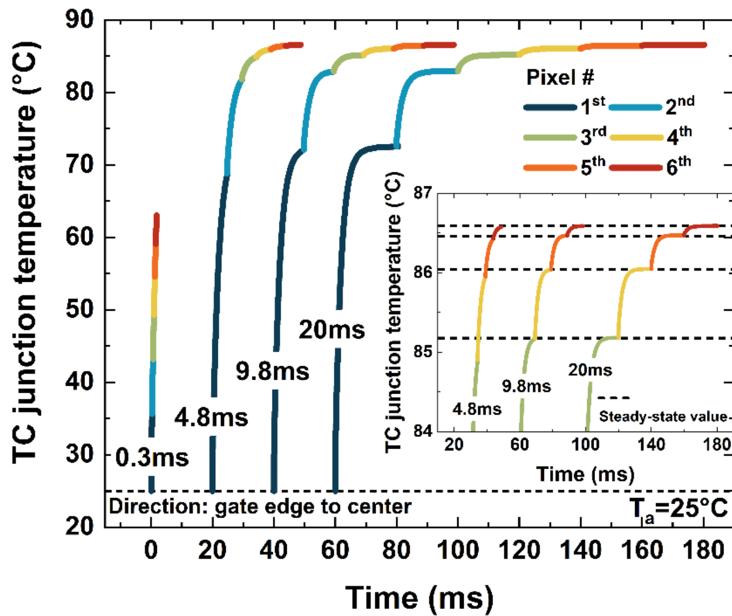

Figure 10. Accumulated simulated transient temperature traces in VTP-200 SThM probe thermocouple, TC, junction for 6 probe displacements (6 pixels) along the passivated gate contact from gate edge towards gate center. Effect of various pixel times (0.3 – 20ms) is presented. Inset shows situation for 3rd-6th pixel in detail to illustrate deviations from steady-state value at the end of each iteration (displacement).

Discussion

By cross-comparison with Raman thermography results obtained on a GaN/SiC HEMT, we confirmed sufficient accuracy and reliability of the SThM as a valid thermography technique, suitable for quantitative studies of the self-heating in (nanoscale) electronic devices. Unprecedented spatial resolution of this technique allows for comprehensive experimental verification of (nanoscale) thermal simulations leading to more accurate temperature predictions for critical applications. By confirming the feasibility of temperature measurements in PeakForce tapping mode in our study, its benefits can be taken advantage of namely (i) the elimination of lateral tip forces for 2D temperature mapping enhancing the spatial resolution, (ii) constant force measurement, (iii) decreased thermal probe wear, and consequently, (iv) more predictable long-term mechanical and thermal contact when compared to contact mode SThM. Our findings, however, showed the actual 2D temperature mapping produced unreliable temperature readings due to the insufficient range of achievable pixel dwell times. The main limitation factor here is the thermal time constant of the SThM probe which reflects its design. Two possible approaches how to address this are: (i) software implementation of low-level control of the probe movement during scanning, allowing for variable time setting probe spends on each pixel, (ii) manual,

point-by-point transient thermal measurement at discrete locations, while dwell times are chosen long enough to suffice the condition of the temperature steady state of the SThM probe.

Here, we chose the latter approach and applied our pixel-by-pixel thermal calibration for each measured location resulting in good agreement with temperatures predicted by the thermal simulation for contact and PF tapping mode SThM.

The rather slow thermal time constant of a typical SThM probe (~1.6ms) limits transient temperature SThM studies to material or device thermal effects with even slower thermal time constants, e.g. measurement of thermal conductivity of thermal insulators or very thick layers, or research of some phase-change materials[47]. Assuming $4\times\tau$ for a thermal system to reach the steady state, ~6.4ms is required for probe to reach it. Based on that, estimated cut-off frequencies in case of pulsed heating experiments fall to the range of 1s-10s Hz. This is impractical for studying of switching electronic devices during pulsed operation as these typically operate at frequencies ranging from few kHz up to RF and therefore predetermines the use of SThM solely for the steady-state device thermography.

Conclusions

Scanning thermal microscopy offers great potential for detailed surface temperature mapping of electronic devices on the nanoscale, but unfortunately it also offers great room for measurement uncertainty and erroneous temperature determination. In this study, we addressed some of the major culprits in SThM responsible for inaccuracies in temperature readings. Understanding of transient thermal response of the SThM probe is one of the key elements for obtaining reliable

2D temperature mapping since the thermal probe is required to reach the temperature steady state at each pixel of the measured map, which is, however, not always possible to achieve in real experimental case. Slow SThM scanning is more favorable, which is somewhat counterintuitive since high speed AFM scanning is readily available nowadays. We created a 3D FE steady-state thermal simulation of the GaN/SiC HEMT and experimentally verified it using Raman thermography measurements; 3D FE transient thermal simulation of a thermal probe was generated including its thermal mass and tip-to-sample thermal resistance, fitted to experimental data. Combining these two models we were able to model probe transient heating during temperature mapping experiments. Resulting accumulated temperature transients demonstrated pixel times >5ms are sufficient for the SThM probe to reach the temperature steady state, for the experimental conditions considered. This was in contrast with the experimental 2D temperature mapping results and pixel dwell times of ~0.1-1s were suggested. Temperature discrepancy of ~15-44% was observed when scanning the sample, however, good agreement was achieved for fixed point measurements.

Acknowledgments

The authors would like to acknowledge financial support from the Engineering and Physical Sciences Research Council (EPSRC) under the program Grant GaN-DaME [grant number EP/P00945X/1]. We thank Ami Chand from AppNano for fruitful discussions.

Appendix A. Supplementary data

Supplementary material related to this article can be found, in the online version, at doi: XYZ

Following content can be found within the Supplementary data file: Illustration of working force ranges for various AFM modes; Experimental data on EMF variation as a function of setpoint;

Details of the study workflow; Material properties used in FE simulations (thermal conductivity, heat capacity, density); Schematic of Raman thermography probed volume; Details of pixel-by-pixel calibration method for 2D temperature mapping; 2D maps showing intercept, slope, standard error, and R^2 - results of linear fitting used in pixel-by-pixel calibration in contact mode SThM.

References

[1] JEDEC, Solid-State Reliability Assessment and Qualification Methodologies (JEP143D), 2019.

[2] W. Kuo, W.-T.K. Chien, T. Kim, Reliability, Yield, and Stress Burn-In, Springer US, Boston, MA, 1998. https://doi.org/10.1007/978-1-4615-5671-8.

[3] S. Vock, O. Escalona, C. Turner, Improving Semiconductor Reliability with Advanced Engineering Methods in Test Program Development, J. Electron. Test. 31 (2015) 107–117. https://doi.org/10.1007/s10836-014-5495-z.

[4] E.K. Sichel, J.I. Pankove, Thermal conductivity of GaN, 25–360 K, J. Phys. Chem. Solids. 38 (1977) 330. https://doi.org/10.1016/0022-3697(77)90112-3.

[5] O. Nilsson, H. Mehling, R. Horn, J. Fricke, R. Hofmann, S. Müller, R. Eckstein, D. Hofmann, Determination of the thermal diffusivity and conductivity of monocrystalline silicon carbide (300-2300 K), High Temp. Press. 29 (1997) 73–79. https://doi.org/10.1068/htec142.

[6] J.W. Pomeroy, M.J. Uren, B. Lambert, M. Kuball, Operating channel temperature in GaN HEMTs: DC versus RF accelerated life testing, in: Microelectron. Reliab., 2015.

https://doi.org/10.1016/j.microrel.2015.09.025.

[7] C.H. Lin, T.A. Merz, D.R. Doutt, M.J. Hetzer, J. Joh, J.A. Del Alamo, U.K. Mishra, L.J. Brillson, Nanoscale mapping of temperature and defect evolution inside operating AlGaN/GaN high electron mobility transistors, Appl. Phys. Lett. 95 (2009) 25–27. https://doi.org/10.1063/1.3189102.

[8] A. Sarua, J. Hangfeng, M. Kuball, M.J. Uren, T. Martin, K.P. Hilton, R.S. Balmer, Integrated micro-Raman/infrared thermography probe for monitoring of self-heating in AlGaN/GaN transistor structures, IEEE Trans. Electron Devices. 53 (2006) 2438–2447. https://doi.org/10.1109/TED.2006.882274.

[9] G. Pavlidis, S. Pavlidis, E.R. Heller, E.A. Moore, R. Vetury, S. Graham, Characterization of AlGaN/GaN HEMTs Using Gate Resistance Thermometry, IEEE Trans. Electron Devices. 64 (2017) 78–83. https://doi.org/10.1109/TED.2016.2625264.

[10] A. Cutivet, F. Cozette, M. Bouchilaoun, A. Chakroun, O. Arenas, M. Lesecq, J.C. De Jaeger, A. Jaouad, F. Boone, H. Maher, Characterization of dynamic self-heating in GaN HEMTs using gate resistance measurement, IEEE Electron Device Lett. 38 (2017) 240–243. https://doi.org/10.1109/LED.2016.2641740.

[11] A. Cutivet, M. Bouchilaoun, B. Hassan, C. Rodriguez, A. Soltani, F. Boone, H. Maher, Thermal Transient Extraction for GaN HEMTs by Frequency-Resolved Gate Resistance Thermometry with Sub-100 ns Time Resolution, Phys. Status Solidi. 1800503 (2018) 1800503. https://doi.org/10.1002/pssa.201800503.

[12] B. Chatterjee, A. Jayawardena, E. Heller, D.W. Snyder, S. Dhar, S. Choi, Thermal

characterization of gallium oxide Schottky barrier diodes, Rev. Sci. Instrum. 89 (2018). https://doi.org/10.1063/1.5053621.

[13] H. Zhou, K. Maize, J. Noh, A. Shakouri, P.D. Ye, Thermodynamic Studies of β-Ga 2 O 3 Nanomembrane Field-Effect Transistors on a Sapphire Substrate, ACS Omega. 2 (2017) 7723–7729. https://doi.org/10.1021/acsomega.7b01313.

[14] M. Kuball, J.W. Pomeroy, A review of raman thermography for electronic and opto-electronic device measurement with submicron spatial and nanosecond temporal resolution, IEEE Trans. Device Mater. Reliab. 16 (2016) 667–684. https://doi.org/10.1109/TDMR.2016.2617458.

[15] M. Kuball, S. Rajasingam, A. Sarua, M.J. Uren, T. Martin, B.T. Hughes, K.P. Hilton, R.S. Balmer, Measurement of temperature distribution in multifinger AlGaN/GaN heterostructure field-effect transistors using micro-Raman spectroscopy, Appl. Phys. Lett. 82 (2003) 124–126. https://doi.org/10.1063/1.1534935.

[16] A. Sarua, A. Bullen, M. Haynes, K. Kuball, High-resolution Raman temperature measurements in GaAs p-HEMT multifinger devices, IEEE Trans. Electron Devices. 54 (2007) 1838–1842. https://doi.org/10.1109/TED.2007.901349.

[17] S. Choi, E.R. Heller, D. Dorsey, R. Vetury, S. Graham, Thermometry of AlGaN/GaN HEMTs using multispectral raman features, IEEE Trans. Electron Devices. 60 (2013) 1898–1904. https://doi.org/10.1109/TED.2013.2255102.

[18] J.W. Pomeroy, M. Bernardoni, D.C. Dumka, D.M. Fanning, M. Kuball, Low thermal resistance GaN-on-diamond transistors characterized by three-dimensional Raman

thermography mapping, Appl. Phys. Lett. 104 (2014). https://doi.org/10.1063/1.4865583.

[19] R.J.T. Simms, J.W. Pomeroy, M.J. Uren, T. Martin, M. Kuball, Channel temperature determination in high-power AlGaN/GaN HFETs using electrical methods and Raman spectroscopy, IEEE Trans. Electron Devices. 55 (2008) 478–482. https://doi.org/10.1109/TED.2007.913005.

[20] M. Kuball, J.W. Pomeroy, F. Gucmann, B. Oner, Thermal analysis of semiconductor devices and materials - Why should I not trust a thermal simulation ?, 2019 IEEE BiCMOS Compd. Semicond. Integr. Circuits Technol. Symp. BCICTS 2019. (2019) 4–8. https://doi.org/10.1109/BCICTS45179.2019.8972763.

[21] R.B. Simon, J.W. Pomeroy, M. Kuball, Diamond micro-Raman thermometers for accurate gate temperature measurements, Appl. Phys. Lett. 104 (2014). https://doi.org/10.1063/1.4879849.

[22] K. Kim, W. Jeong, W. Lee, P. Reddy, Ultra-high vacuum scanning thermal microscopy for nanometer resolution quantitative thermometry, ACS Nano. 6 (2012) 4248–4257. https://doi.org/10.1021/nn300774n.

[23] G.S. Shekhawat, S. Ramachandran, H. Jiryaei Sharahi, S. Sarkar, K. Hujsak, Y. Li, K. Hagglund, S. Kim, G. Aden, A. Chand, V.P. Dravid, Micromachined Chip Scale Thermal Sensor for Thermal Imaging, ACS Nano. 12 (2018) 1760–1767. https://doi.org/10.1021/acsnano.7b08504.

[24] L. Ramiandrisoa, A. Allard, Y. Joumani, B. Hay, S. Gomés, L. Ramiandrisoa, A. Allard, Y. Joumani, B. Hay, A dark mode in scanning thermal microscopy, 125115 (2017).

[25] K. Kim, J. Chung, J. Won, O. Kwon, J.S. Lee, S.H. Park, Y.K. Choi, Quantitative scanning thermal microscopy using double scan technique, Appl. Phys. Lett. 93 (2008) 1–4. https://doi.org/10.1063/1.3033545.

[26] A. Soudi, R.D. Dawson, Y. Gu, Quantitative Heat Dissipation Scanning Thermal Microscopy and Nanowires Probed by Combining Characteristics in Current-Carrying GaN Spatially Resolved Raman Spectroscopy, ACS Nano. 5 (2011) 255–262.

[27] F. Menges, P. Mensch, H. Schmid, H. Riel, A. Stemmer, B. Gotsmann, Temperature mapping of operating nanoscale devices by scanning probe thermometry, Nat. Commun. 7 (2016) 1–6. https://doi.org/10.1038/ncomms10874.

[28] F. Menges, H. Riel, A. Stemmer, B. Gotsmann, Quantitative thermometry of nanoscale hot spots, Nano Lett. 12 (2012) 596–601. https://doi.org/10.1021/nl203169t.

[29] R. Aubry, J. Jacquet, J. Weaver, O. Durand, P. Dobson, G. Mills, M. Forte-poisson, S. Cassette, S. Delage, SThM Temperature Mapping and Nonlinear Thermal Resistance Evolution With Bias on AlGaN/GaN HEMT Devices, IEEE Trans. Electron Devices. 54 (2007) 385–390.

[30] P.D. Tovee, M.E. Pumarol, M.C. Rosamond, R. Jones, M.C. Petty, D.A. Zeze, O. V. Kolosov, Nanoscale resolution scanning thermal microscopy using carbon nanotube tipped thermal probes, Phys. Chem. Chem. Phys. 16 (2014) 1174–1181. https://doi.org/10.1039/C3CP53047G.

[31] M.M. Sadeghi, S. Park, Y. Huang, D. Akinwande, Z. Yao, J. Murthy, L. Shi, Quantitative scanning thermal microscopy of graphene devices on flexible polyimide substrates, J. Appl.

Phys. 119 (2016). https://doi.org/10.1063/1.4953584.

[32] E. Yalon, S. Deshmukh, M. Muñoz Rojo, F. Lian, C.M. Neumann, F. Xiong, E. Pop, Spatially Resolved Thermometry of Resistive Memory Devices, Sci. Rep. 7 (2017) 1–9. https://doi.org/10.1038/s41598-017-14498-3.

[33] K. Nakanishi, A. Kogure, R. Kuwana, H. Takamatsu, K. Ito, Development of a novel Scanning Thermal Microscopy （SThM） method to measure the thermal conductivity of biological cells, Biocontrol Sci. 22 (2017) 175–180. https://doi.org/10.4265/bio.22.175.

[34] S.B. Kaemmer, Introduction to ScanAsyst and PeakForce Tapping, 2011.

[35] Bruker, PeakForce Tapping - How AFM Should Be, 2015. https://www.bruker.com/products/surface-and-dimensional-analysis/atomic-force-microscopes/modes/modes/imaging-modes/peakforce-tapping/overview.html.

[36] V.V. Tsukruk, S. Singamaneni, Basics of Atomic Force Microscopy Studies of Soft Matter, in: V.V. Tsukruk, S. Singamaneni (Eds.), Scanning Probe Microsc. Soft Matter, Wiley-VCH Verlag GmbH & Co. KGaA, 2011. https://doi.org/10.1002/9783527639953.ch3.

[37] Y. Ge, Y. Zhang, J.M.R. Weaver, H. Zhou, P.S. Dobson, Topography-free sample for thermal spatial response measurement of scanning thermal microscopy, J. Vac. Sci. Technol. B, Nanotechnol. Microelectron. Mater. Process. Meas. Phenom. 33 (2015) 06FA03. https://doi.org/10.1116/1.4933172.

[38] S. Gomès, A. Assy, P.O. Chapuis, Scanning thermal microscopy: A review, Phys. Status Solidi Appl. Mater. Sci. 212 (2015) 477–494. https://doi.org/10.1002/pssa.201400360.

[39] B. Shi, X. Tang, T. Lu, T. Nakayama, Y. Li, J. Zhou, Interfacial thermal conductance at metal-nonmetal interface via electron-phonon coupling, Mod. Phys. Lett. B. 32 (2018) 1–29. https://doi.org/10.1142/S0217984918300041.

[40] D. Singh, J.Y. Murthy, T.S. Fisher, Effect of phonon dispersion on thermal conduction across Si/Ge interfaces, J. Heat Transfer. 133 (2011). https://doi.org/10.1115/1.4004429.

[41] H. Wang, Y. Xu, M. Shimono, Y. Tanaka, M. Yamazaki, Computation of interfacial thermal resistance by phonon diffuse mismatch model, Mater. Trans. 48 (2007) 2349–2352. https://doi.org/10.2320/matertrans.MAW200717.

[42] AppNano, Catalog of SPM Probes and Accessories, (2017). http://www.appnano.com/download/catalog_120817.pdf.

[43] G.S. Shekhawat, S. Ramachandran, H.J. Sharahi, S. Sarkar, V.P. Dravid, Supporting information: Micromachined Chip Scale Thermal Sensor for Thermal Imaging, ACS Nano. 12 (2018) 1760–1767. https://doi.org/10.1021/acsnano.7b08504.

[44] B.A. Danilchenko, T. Paszkiewicz, S. Wolski, A. Jezowski, T. Plackowski, Heat capacity and phonon mean free path of wurtzite GaN, Appl. Phys. Lett. 89 (2006) 1–4. https://doi.org/10.1063/1.2335373.

[45] L. Shi, A. Majumdar, Thermal transport mechanisms at nanoscale point contacts, J. Heat Transfer. 124 (2002) 329–337. https://doi.org/10.1115/1.1447939.

[46] K.R. Bagnall, E.N. Wang, Theory of Thermal Time Constants in GaN High-Electron-Mobility Transistors, IEEE Trans. Components, Packag. Manuf. Technol. 8 (2018) 606–620. https://doi.org/10.1109/TCPMT.2017.2773065.

[47] L. Ghadbeigi, B. Day, K. Lundgren, T.D. Sparks, Cold temperature performance of phase change material based battery thermal management systems, Energy Reports. 4 (2018) 303–307. https://doi.org/10.1016/j.egyr.2018.04.001.